

Porous glass electroosmotic pumps: theory

Shuhuai Yao and Juan G. Santiago*

Department of Mechanical Engineering, Stanford University, Stanford, CA 94305, USA

Received 17 January 2003; accepted 17 July 2003

Abstract

This paper presents an analytical study of electroosmotic (EO) pumps with porous pumping structures. We have developed an analytical model to solve for electroosmotic flow rate, pump current, and thermodynamic efficiency as a function of pump pressure load for porous-structure EO pumps. The model uses a symmetric electrolyte approximation valid for the high-zeta-potential regime and numerically solves the Poisson–Boltzmann equation for charge distribution in the idealized pore geometry. Generalized scaling of pumping performance is discussed in the context of a parameterization that includes porosity, tortuosity, pore size, bulk ionic density, and the nonuniform conductivity distribution over charge layers. The model also incorporates an approximate ionic-strength-dependent zeta potential formulation.

© 2003 Elsevier Inc. All rights reserved.

Keywords: Electroosmotic pump; Porous glass; Thermodynamic efficiency; Zeta potential

1. Introduction

EO pumps are devices that generate both flow rate and significant pressure capacity using electroosmosis through pores or channels. The term electroosmosis refers to the bulk motion of an electrolyte caused by Coulombic forces acting on diffuse ions near a flow channel's solid/liquid interface [1]. Although electroosmosis has been studied for nearly two centuries [2], its application to miniaturized devices for the generation of high-pressure flow streams has been of interest only in the last three decades. Electroosmotic (EO) pumps have no moving parts and offer distinct advantages over other micropumps including high pressure (well over one atmosphere of pressure is readily achievable at 100 V) and large flow rate (greater than 30 ml/min at 100 V). These devices have the potential to impact a variety of applications including microelectronics cooling and bio-analytical applications [3–5]. Interest in this research area is increasing.

In 1974, Pretorius et al. [6] first described using electroosmotic flow to drive a liquid chromatographic separation as an alternative to high-pressure pumping, but did not demonstrate the ability to generate high pressure. They demonstrated a flow velocity of 0.2 mm/s at a field of 2000 V/cm

in 5-cm-long, 1-mm-inner-diameter glass columns packed with polydisperse silica particles with dimensions ranging from 1 to 20 μm . We estimate that their porous structure should have been able to generate pressures in excess of 40 atm at a 1-kV applied potential. That same year, Theeuwes [7,8] patented and reduced to practice the concept of miniaturized electroosmotic pumps for the generation of relatively high-pressure flow streams and discussed their application to a variety of controlled drug delivery systems. Glass frits 0.2 cm thick with pore diameter 0.1 μm were used as the pumping medium, and they demonstrated a flow rate of 8.3×10^{-2} $\mu\text{l}/\text{min}$ (for applied field 160 V/cm) and a pressure capacity of 0.7 atm at 50 V. Theeuwes noted that pump pressure is linearly dependent on applied voltage. Two and a half decades later, Gan and co-workers [9,10] described the development of a borosilicate porous glass EO pump device with pore diameter 2–5 μm fabricated using high-temperature sintering. They demonstrated the pumping of several fluid chemistries and the effect of these chemistries on flow stability. Their pump generated 3.5 ml/min and 1.5 atm at 500 V. Two years later, Paul and Rakestraw [11] built packed-column EO pumps and demonstrated that large (12-kV) applied potentials could be used to generate pressure capacities of 340 atm using a 75- μm inner diameter capillary packed with 3- μm -diameter beads. They used a fabrication method similar to that of Yan [12] for electrochromatographic columns. Extrapolation of this performance suggests the flow rates of these pumps

* Corresponding author.

E-mail address: juan.santiago@stanford.edu (J.G. Santiago).

were 100 $\mu\text{l}/\text{min}$ for 10-kV applied potentials. Paul and co-workers patented the use of these pumps as miniaturized actuation devices and high-pressure valves [13,14]. Zeng et al. [15] presented an analytical model and characterization of EO pumps fabricated by packing 3.5- μm -diameter beads in fused silica capillaries with inner diameters of 530 μm . These pumps achieved maximum pressure and flow rates of 23.5 atm and 4.8 $\mu\text{m}/\text{min}$, respectively, at 2-kV potentials. In an effort to increase the flow rate of such pumps, Zeng et al. [16] used polymerized frit structures and slurry packing of nonporous silica particles to demonstrate EO pumps that delivered maximum flow rates and pressures of 0.8 ml/min and 2.0 atm, respectively, at 1.0 kV. More recently, we demonstrated sintered glass frit pumps that provide maximum flow rates and pressure capacities on the order of 7 ml/min and 2.5 atm, respectively, at 200 V, with an active pumping volume of less than 2 cm^3 [17]. In parallel efforts, Chen and Santiago [18] and Laser et al. [19] demonstrated EO pumps fabricated using planar micromachined structures in glass and silicon substrates, respectively. Chen and Santiago also presented an analytical model for the estimation of thermodynamic efficiency in these “slot” structure pumps, including a detailed energy balance of a pump and load closed-loop system.

Despite the conference, journal, and patent literature described above, research work on EO pumps has not yet provided full insight into the operational behavior and fundamental flow principles behind EO pumps. In particular, generalized scaling (e.g., geometric scaling) analyses, detailed models of electrical double layer (EDL) physics, advective current effects, and thermodynamic efficiency models have not been presented. In this study, we present an analytical and numerical model that can be used to predict pump flow rate, pressure, and thermodynamic efficiency across variations in geometry, applied potentials, working fluid chemistry, and pressure load conditions. The model treats the porous pumping structure of the pump as a network of many flow channels in parallel and the case of electrical double layers with a thickness on the order of the capillary radius (in this paper we refer to this regime as “finite electrical double layers”). We have used this model to guide the design of our EO pumps for high-heat-load heat transfer applications [3].

2. Theory

2.1. Electroosmotic flow model

We treat electroosmotic flow (EOF) in porous media as flow through a large number of idealized tortuous microchannels in parallel, as depicted schematically in Fig. 1. In this model, tortuous microchannels (i.e., pores) with circular cross sections are assumed to have equal pore radii, a , and an equal value of zeta potential, ζ . The channels have a tortuosity τ and the porous pumping structure has a porosity ψ . This model is suggested by the work of Mazur

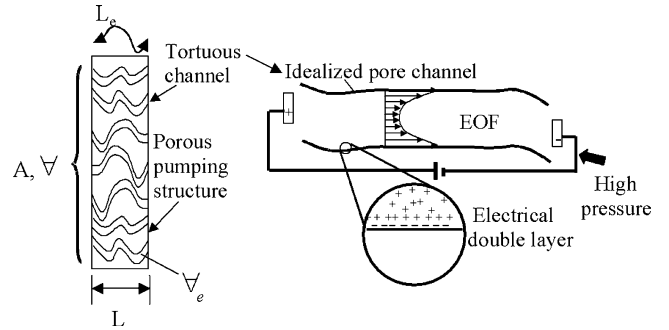


Fig. 1. Schematic of the porous pump model with idealized cylindrical pores of uniform diameter. Flow is modeled within each pore (as shown on the right) and then flow rate and current are integrated over all pores in the system. The structure can be characterized by its total volume, V , the void volume, V_e , its length L , and the tortuous characteristic length of the pores L_e . The ratios V_e/V and $(L_e/L)^2$ are defined as the porosity and tortuosity, respectively.

and Overbeek [20], which leveraged a similar formulation for electroosmotic flow in porous diaphragm structures. The model can be used to derive a set of flow equations that are similar to the corresponding equations for EOF in a single capillary [21]. By applying both a pressure load and potential gradients along the axes of the pores of the pumping structure, expressions can be derived for the velocity field in a single cylindrical pore [21]. Implicitly, in terms of the electric potential within the pore, the general velocity profile within the circular cross section of a pore with a high axial-length-to-radius ratio is

$$u(r) = -\frac{a^2 P_x}{4\mu} \left(1 - \frac{r^2}{a^2}\right) - \frac{\varepsilon \zeta E_x}{\mu} \left(1 - \frac{\varphi}{\zeta}\right). \quad (1)$$

Here, $P_x = \Delta P/L_e$ is the streamwise pressure gradient and $E_x = V_{\text{eff}}/L_e$ is the streamwise electric field within the pores. The calculation of flow rate and pressure drop therefore reduces to finding an adequate model for the potential distribution associated with the EDL in the pore. This velocity profile can be integrated over the cross-sectional area, A , and axial length of the porous material, L , to yield the following expression for the flow rate of the entire structure [15,17],

$$Q = \frac{\psi}{\tau} \left[-\frac{\Delta P A a^2}{8\mu L} - \frac{\varepsilon \zeta A V_{\text{eff}}}{\mu L} f \right], \quad (2)$$

where A is the cross-sectional area of the porous structure, $\tau = (L_e/L)^2$ is the tortuosity, and $\psi = V_e/V$ is the porosity. We define L_e as the characteristic length of travel for flow along the pore path and L as the physical length of the porous pumping structure. V_e and V are the void and total volumes of the porous medium, respectively. The term on the right contains the integral

$$f = \int_0^a \left(1 - \frac{\varphi}{\zeta}\right) \frac{2r}{a^2} dr. \quad (3)$$

The solution to this integral can be determined by solving the Poisson–Boltzmann (PB) equation for the potential, where

$$\nabla^2\varphi = \frac{1}{r} \frac{d}{dr} \left(r \frac{d\varphi}{dr} \right) = -\frac{1}{\varepsilon} \sum_i n_{\infty,i} z_i e \exp\left(-\frac{z_i e\varphi}{kT}\right). \quad (4)$$

The correct formulation for the model depends on the type of buffer used and the magnitude of the zeta potential of the EDL [1]. The zeta potential of the glass pumping structures of interest here are typically of order 100 mV which is significantly higher than the term ze/kT (equal to 25.7 mV for $z = 1$ at $T = 20^\circ\text{C}$) in the exponential functions above. As suggested by Verwey and Overbeek [22] and Hunter [1], electrokinetic systems with such potential distributions can be treated as having symmetric electrolytes with the properties of the counterion (in our case, the sodium ions of our sodium tetraborate buffer). The physical interpretation of this approach is that, at zeta potential values well above 25.7 mV, the potential distribution in the EDL is determined mostly by the attraction of counterions to the charged wall, while the repulsion of co-ions is less important [1]. For high zeta potential, the counterion density near the wall is significantly higher than that of the co-ion density. In this paper, we will treat our buffers as symmetric, monovalent electrolytes with the properties of the sodium ion in determining Debye lengths and potential distributions. In determining total pump current, we will use the charge distributions obtained with this model for the advective current component, and measured values of bulk conductivity to estimate electromigration outside of the EDL. This treatment of the bulk conductivity leverages a single measurement to account for all of the ions (and their respective ionic mobilities) present in the buffer.

For a symmetric electrolyte with $z_+ = -z_-$, the PB equation can be expressed as

$$\frac{1}{r} \frac{d}{dr} \left(r \frac{d\varphi}{dr} \right) = \frac{2n_{\infty}ze}{\varepsilon} \sinh\left(\frac{ze\varphi}{kT}\right). \quad (5)$$

The solution to this nonlinear equation was obtained numerically using a substitution of the form $\varphi = 4 \operatorname{arctanh}(\phi)$, as suggested by Bowen and Jenny [23]. The resulting equation is also nonlinear but less stiff. We employed a fourth-order Runge–Kutta algorithm [24] with a shooting procedure to solve this boundary value problem. The numerical solution for φ is plotted in Fig. 2. As a comparison, we also present in Fig. 2 a solution to a linearized form of Eq. (5), where the term $\sinh(ze\varphi/kT)$ is approximated as $ze\varphi/kT$ ($= \varphi^*$). This linearization is the so-called Debye–Hückel approximation valid for small zeta potentials, which results in a second-order-accurate formulation of Eq. (5) for a symmetric electrolyte. Rice and Whitehead [21] first used this approximation to solve for potential distributions in cylindrical tubes, which yields simply $\varphi = \zeta I_0(r^*)/I_0(a^*)$, where I_0 is the zero-order modified Bessel function of the first kind. The nondimensionalization in this solution is as follows: $r^* = r/\lambda$ and $a^* = a/\lambda$. λ is the Debye length which, for a symmetric electrolyte is $(\varepsilon kT/2e^2 z^2 n_{\infty})^{0.5}$. As shown

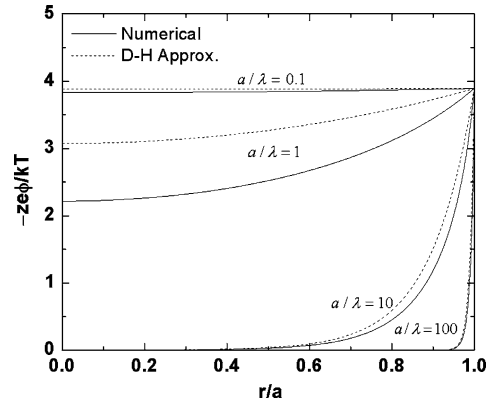


Fig. 2. Numerical solution to the Poisson–Boltzmann equation (Eq. (5)) for a symmetric electrolyte, shown together with the analytical solution to the linearized Debye–Hückel approximation. The Debye–Hückel approximation is accurate only for ratios of a/λ of order 100 or larger, and for values of a/λ of order 0.1 and lower.

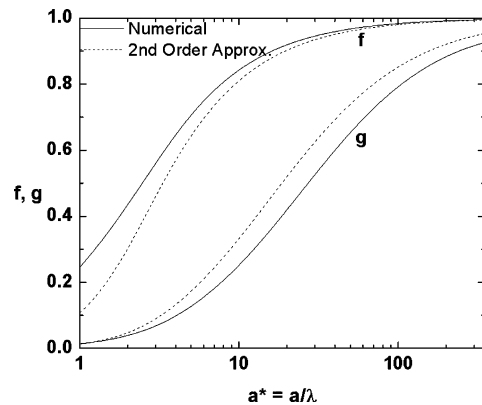


Fig. 3. Nondimensional model parameters f and g as a function of nondimensional pore size. The plots are generated using sample parameter values of $\zeta^* = -3.9$ and $\beta = 6.8$ assuming a typical zeta potential value of 100 mV.

in Fig. 2, discrepancy between the numerical and linearized solutions is particularly apparent for values of a^* of order unity.

Given the numerical solution for the potential, the integral in the flow rate expression, f , can also be calculated numerically (using a simple Simpson’s rule integration scheme), and the result is plotted in Fig. 3. Shown together with this numerical solution is the Debye–Hückel approximation resulting from an integration of Eq. (3), where

$$f(a^*) \cong 1 - \frac{2I_1(a^*)}{a^*I_0(a^*)}. \quad (6)$$

I_1 is a first-order modified Bessel function of the first kind. As shown in the plot, the results show the discrepancy between the two solutions for a zeta potential value of 100 mV, which is typical of our electroosmotic pumps. As expected, both the numerical and linearized solutions of f tend to unity for large a^* systems which have uniform fluid velocity throughout most of the flow cross section. The behavior at low a^* , however, highlights the important difference be-

tween the two solutions and shows how the linearized solution underpredicts pump flow rate performance.

The maximum flow rate, Q_{\max} , and maximum pressure, ΔP_{\max} , of the pump are derived from Eq. (2) as

$$Q_{\max} = -\frac{\psi}{\tau} \frac{\varepsilon \zeta A V_{\text{eff}}}{\mu L} f, \quad (7)$$

$$\Delta P_{\max} = -\frac{8\varepsilon \zeta V_{\text{eff}}}{a^2} f. \quad (8)$$

These equations show that, for a given value of f , high electric fields and large cross-sectional areas lead to high flow rate, while pressure performance is linked to small pore diameters and high voltage. This formulation can be nondimensionalized as

$$V_{\text{eff}}^* = -\frac{V_{\text{eff}}}{\zeta}, \quad (9)$$

$$E_{\text{eff}}^* = -\frac{V_{\text{eff}} \lambda}{\zeta L}, \quad (10)$$

$$Q_{\max}^* = \frac{Q_{\max} \mu \lambda}{\varepsilon \zeta^2 A}, \quad (11)$$

$$\Delta P_{\max}^* = \frac{\Delta P_{\max} a^2}{8\varepsilon \zeta^2}, \quad (12)$$

so that the equations become

$$Q_{\max}^* = \frac{\psi}{\tau} f E_{\text{eff}}^*, \quad (13)$$

$$\Delta P_{\max}^* = f V_{\text{eff}}^*. \quad (14)$$

Equations (7) and (8) give the ratio

$$\kappa = \frac{Q_{\max}}{\Delta P_{\max}} = \frac{\psi}{\tau} \frac{A a^2}{8\mu L}. \quad (15)$$

The parameter κ can be useful in determining the tortuosity of the pump experimentally from pressure and flow rate measurements and is independent of pump zeta potential. For example, ψ can be obtained using dry and wet weight measurements of the porous structure and a can be estimated using mean pore radius measurements performed using a mercury intrusion porosimeter [25]. Given these parameters and a measurement of temperature during experiments of Q_{\max} , and ΔP_{\max} (to calculate the value of the bulk viscosity μ), Eq. (15) can be used to estimate τ .

2.2. Electrical current in electroosmotic flow

In this paper, we present the derivation of an expression that can be used to predict total current in an EO pump using a symmetric electrolyte model. As discussed by Rice and Whitehead [21], the total current in an electroosmotic pumping channel is the sum of advective and electromigration currents I_{adv} and I_{em} , respectively, for the typical case of negligible ion diffusion. In the electromigration component, Rice and Whitehead made the very rough approximation that ion conductivity throughout the cross-section of the pore is uniform throughout the fluid up to the wall of the

capillary and made no allowance for the modified ionic concentration in the electric double layer (EDL) near the wall. Such an assumption is justified when zeta potential is low (e.g., $|\varphi^*| < 1$) and the molar conductivities of cations and anions are approximately equal (e.g., as in the case of simple KCl electrolytes). However, as suggested by the work of Morrison and Osterle [26], we can derive the advective and electromigration components of current from the charge distribution, velocity field, and conductivity distribution within the pores as

$$I_{\text{adv}} = 2\pi \int_0^a u(r) \rho(r) r dr, \quad (16)$$

$$I_{\text{em}} = 2\pi \int_0^a [\sigma(r) E_x] r dr, \quad (17)$$

where $\rho(r)$ is the charge density at a point distance r from the axis and $\sigma(r)$ is the conductivity at this point. For finite values of φ^* and symmetric electrolytes in which the molar conductivities of cations and anions can be individually specified, the charge density and conductivity terms can be written as

$$\rho(r) = -\frac{\varepsilon}{r} \frac{d}{dr} \left(r \frac{d\varphi}{dr} \right), \quad (18)$$

$$\sigma(r) = c_{\infty} \left[\Lambda_+ \exp\left(-\frac{ze\varphi}{kT}\right) + \Lambda_- \exp\left(\frac{ze\varphi}{kT}\right) \right], \quad (19)$$

where Λ_+ and Λ_- are the cation and anion molar conductivities, respectively. Note that these expressions for ρ and σ can be approximated using Taylor series expansions of the sinh term in Eq. (5) and the exponents in Eq. (19). To second-order accuracy, the advective and electromigration current densities, i , in the channel are then

$$i_{\text{adv}} = \frac{\varepsilon \zeta P_x a^2}{4\mu \lambda^2} \left(1 - \frac{r^2}{a^2} \right) \frac{I_0(r)}{I_0(a)} + \sigma_{\infty} E_x \beta \frac{I_0(r)}{I_0(a)} \left[1 - \frac{I_0(r)}{I_0(a)} \right], \quad (20)$$

$$i_{\text{em}} = \sigma_{\infty} E_x \left[1 - \frac{\zeta^* (\Lambda_+ - \Lambda_-)}{\Lambda} \frac{I_0(r)}{I_0(a)} + \frac{\zeta^{*2}}{2} \frac{I_1^2(r)}{I_0^2(a)} \right], \quad (21)$$

where

$$\zeta^* = \frac{ze\zeta}{kT}, \quad \beta = \frac{\varepsilon^2 \zeta^2}{\mu \sigma_{\infty} \lambda^2}.$$

In Eq. (21), $\Lambda = \Lambda_+ + \Lambda_-$. The parameter β can be interpreted as the ratio of EOF advective current to electromigration current, and describes the maximum advective current density associated with EOF. In applying these simple, symmetric electrolyte equations for current density to our buffered electrolyte case, we use the valence of the sodium ion (+1) and the molar conductivity of the sodium ion: $\Lambda_+ = 5 \times 10^{-3} \text{ S m}^2/\text{mol}$ [27]. Conductivity measurements show that our bulk solution, sodium tetraborate buffer, has

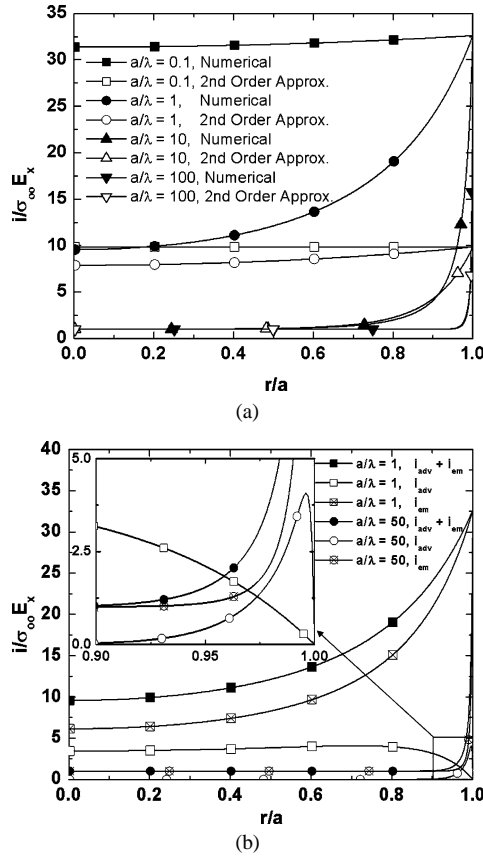


Fig. 4. Variation of current density across a single cylindrical pore with $P_x = 0$ for nominal values of $\zeta^* = -3.9$ and $\beta = 6.8$. (a) Numerical solution for total current density is compared with the second-order approximations given by Eqs. (20) and (21). (b) Numerical solution of the contributions of advective current, and electromigration current, along with total current distribution, for $a/\lambda = 1$ and 50 .

a nominal conductivity of $\Lambda = 7.5 \times 10^{-3} \text{ S m}^2/\text{mol}$ [28], so that the effective molar conductivity of buffer ions other than sodium (e.g., $\text{B}(\text{OH})_4^-$ and $\text{B}_3\text{O}_3(\text{OH})_4^-$) was estimated as $\Lambda_- = 2.5 \times 10^{-3} \text{ S m}^2/\text{mol}$.

Figure 4a shows the variation of the total current density across a single capillary from the PB solution in Fig. 2 for the case of zero pressure gradients ($P_x = 0$). In this calculation, we assume a typical zeta-potential value of 100 mV and typical parameter values of $\zeta^* = -3.9$ and $\beta = 6.8$. Shown together with the numerical solution are the approximate expressions Eqs. (20) and (21). The second-order-accurate expressions for current density clearly underpredict the conductivity in the EDL for finite values of φ^* . Figure 4b shows the individual contributions of advective and electromigration current as derived from the numerical solution of the nonlinear PB equation. The advective current component decreases to zero at the wall because of the imposed no-slip condition on liquid motion. The electromigration current component is proportional to local ion density and so increases as r^* approaches unity. The EDL can have a significant effect on current densities and area-average current density can be a strong function of a^* .

The total current in a single pore is obtained by integration of Eqs. (16) and (17) (which are respectively area integrals of Eqs. (20) and (21)) to yield

$$I_p = \frac{\pi a^2 \varepsilon \zeta P_x}{\mu} \int_0^a \left(1 - \frac{\varphi}{\zeta}\right) \frac{2r}{a^2} dr + \frac{\pi a^2 \varepsilon^2 E_x}{\mu} \int_0^a \left(\frac{d\varphi}{dr}\right)^2 \frac{2r}{a^2} dr + \pi a^2 c_\infty E_x \int_0^a \left[\Lambda_+ \exp\left(-\frac{ze\varphi}{kT}\right) + \Lambda_- \exp\left(\frac{ze\varphi}{kT}\right) \right] \frac{2r}{a^2} dr. \quad (22)$$

The first term in Eq. (22) is the advective current which is proportional to the pressure gradient, P_x , and the second term is the advective current due to EOF, and the third is the electromigration current. The total current through all of the pores is obtained by integrating Eq. (22) over the flow cross-section of the porous structure to obtain

$$I = \frac{\psi A}{\sqrt{\tau} \pi a^2} I_p. \quad (23)$$

We can now derive another relation which is useful in experimental characterizations of pump parameters and is expressed in terms of pump flow rate and current. Because of the effects of advective current, the total current of an EO pump is expected to be a linear function of backpressure. The maximum current I_{\max} is therefore obtained at the point where $\Delta P = 0$ (assuming $\Delta P \geq 0$). Combining Eqs. (7) and (23),

$$\frac{Q_{\max}}{I_{\max}} = -\frac{\varepsilon \zeta}{\mu \sigma_\infty} g, \quad (24)$$

where

$$g = f \left/ \left\{ \frac{\beta}{\zeta^* 2} \int_0^{a^*} \left(\frac{d\varphi^*}{dr^*}\right)^2 \frac{2r^*}{a^{*2}} dr^* + \int_0^{a^*} \left[\frac{\Lambda_+}{\Lambda} \exp(-\varphi^*) + \frac{\Lambda_-}{\Lambda} \exp(\varphi^*) \right] \frac{2r^*}{a^{*2}} dr^* \right\} \right. \quad (25)$$

The expression of Eq. (25) was evaluated using the numerical scheme described earlier with nominal parameter values of $\zeta^* = -3.9$, $\beta = 6.8$. The results are plotted in Fig. 3. The dimensionless flow rate per current ratio, g , reduces to zero for small nondimensional pore diameters as electromigration ion fluxes per unit area are very high in that regime, while flow rate per unit area is greatly reduced from the case of infinitesimal EDLs. g also displays anticipated trends to unity for large a^* . Shown together with the numerical solution for g is the small potential, second order accurate approximation of the PB equation, in which

Eq. (25) can be derived analytically as follows:

$$g(a^*, \zeta^*, \beta) \cong f(a^*) \left/ \left\{ \beta \left[\frac{I_1^2(a^*) - I_0(a^*)I_2(a^*)}{I_0^2(a^*)} \right] + 1 - \frac{\zeta^*(\Lambda_+ - \Lambda_-)}{\Lambda} \frac{I_1(a^*)}{a^* I_0(a^*)} + \frac{\zeta^{*2}}{2} \left[1 - \frac{I_1^2(a^*)}{I_0^2(a^*)} \right] \right\} \right. \quad (26)$$

Note the discrepancy between the numerical and the second-order approximated solutions for g and the second-order approximation can overpredict the parameter g by 30%. These trends have important consequences in the determination of flow rate and thermodynamic efficiency of the pump. In particular, Eq. (22) allows for the estimation for ζ of the pump flow rate and current measurements at the zero pressure gradient condition (and estimates of the fluid properties μ , ε , and σ_∞). This method is used to characterize the performance of our EO pumps in Yao et al. [28].

The maximum total current can be nondimensionalized as

$$I_{\max}^* = -\frac{I_{\max}\lambda}{\sigma_\infty \zeta A}, \quad (27)$$

which also yields a relationship for the nondimensional electrical field,

$$I_{\max}^* = \frac{\psi}{\tau} \frac{f}{g} E_{\text{eff}}^*. \quad (28)$$

Last, we can derive for the nonlinear problem a relation for the ratio of the maximum values of the advected current to the total current in a pump:

$$\frac{I_{\max, \text{adv}}}{I_{\max}} = \left\{ \frac{\beta}{\zeta^{*2}} \int_0^{a^*} \left(\frac{d\varphi^*}{dr^*} \right)^2 \frac{2r^*}{a^{*2}} dr^* \right\} \left/ \left\{ \frac{\beta}{\zeta^{*2}} \int_0^{a^*} \left(\frac{d\varphi^*}{dr^*} \right)^2 \frac{2r^*}{a^{*2}} dr^* + \int_0^{a^*} \left[\frac{\Lambda_+}{\Lambda} \exp(-\varphi^*) + \frac{\Lambda_-}{\Lambda} \exp(\varphi^*) \right] \frac{2r^*}{a^{*2}} dr^* \right\} \right. \quad (29)$$

These current maxima occur in the case of zero pressure load. This current ratio is strongly dependent on a^* and weakly dependent on ζ . As shown in Fig. 5, the numerical solution of this ratio as a function of a^* is similar in shape to the thermodynamic efficiency (discussed in detail in the next section) but with a peak value of 0.29 at $a^* = 4$ and which asymptotes to zero for large values of a^* . The expected theoretical, area-averaged advective current can be as much as 29% of the total current.

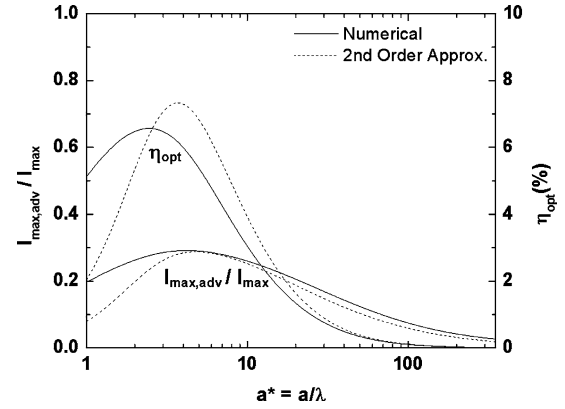


Fig. 5. Advective–total maximum current ratio, $I_{\max, \text{adv}}/I_{\max}$, and thermodynamic efficiency, η_{opt} , as a function of nondimensional pore size for $\zeta^* = -3.9$ and $\beta = 6.8$.

2.3. Thermodynamic efficiency of porous EO pumps

An analysis of the thermodynamic efficiency of a planar EO pump has been presented recently by Chen and Santiago [18]. Their model applies a Debye–Hückel approximation and uses a measured value of zeta potential on the silica/symmetric electrolyte interface as an input variable. Here we present three extensions to their formulation including a numerical solution for the PB potential formulation (to account for finite values of φ^*), the effects of advective current (which are significant in our current pump structures), and an evaluation of the operational point of maximum efficiency. Thermodynamic efficiency is defined as the useful pressure work delivered by the pump over the total power consumption,

$$\eta = \frac{W_P}{V_{\text{app}} I} = \frac{\Delta P Q}{V_{\text{app}} I}, \quad (30)$$

where V_{app} and I are the voltage and the current in the main circuit. The total power consumption is expressed as the sum of pressure work, viscous dissipation and electrical dissipation. As described by Chen and Santiago, the power consumption associated with dissociation of water molecules (electrolysis) at the electrodes is typically negligible compared to the overall power dissipated by the pump and is not included in the formulation.

Combining Eqs. (2), (23), and (30) above, the thermodynamic efficiency can be derived as

$$\eta = \frac{(1 - \Delta P') \Delta P'}{(\theta/4) - \Delta P'}, \quad (31)$$

where

$$\theta = \frac{V_{\text{app}} a^{*2}}{V_{\text{eff}} 2\beta f g}. \quad (32)$$

Here pressure is normalized as $\Delta P' = \Delta P / \Delta P_{\max}$. The θ parameter takes into account the loss in efficiency due to the electrode-to-frit voltage drop (quantified by $V_{\text{app}}/V_{\text{eff}}$) and the effects of the EDL on flow rate, pressure, and current generation. Although Q is a linear function of ΔP ,

the maximum value of η is not simply the point where $\Delta P = \Delta P_{\max}/2$ since the total current, I , in the denominator of Eq. (30) is also a function of pressure load. The optimal point of operation can be determined by formulating the partial derivative of Eq. (31) with respect to $\Delta P'$ while holding θ constant to obtain

$$\Delta P' = \frac{\theta}{4} - \sqrt{\frac{\theta^2}{16} - \frac{\theta}{4}}. \quad (33)$$

Expanding the right hand side of Eq. (33) in a Taylor series, we have

$$\Delta P' = \frac{\theta}{4} \left(1 - \sqrt{1 - \frac{4}{\theta}} \right) \cong \frac{\theta}{4} \left[\frac{2}{\theta} + \frac{2}{\theta^2} + O\left(\frac{1}{\theta^3}\right) \right]. \quad (34)$$

Taking a second-order-accurate approximation of this relation, the optimum pressure condition is

$$\Delta P'_{\text{opt}} \cong \frac{1}{2} + \frac{1}{2\theta} \quad (35)$$

and the optimal efficiency is then, to second order,

$$\eta_{\text{opt}} \cong \frac{\theta^2 - 1}{\theta^3 - 2\theta^2 - 2\theta}. \quad (36)$$

For thin EDL systems with θ much greater than unity, a first-order-accurate expression of $\Delta P' = 0.5$ can be used (so that the optimum pressure is $\Delta P_{\max}/2$). For this simple case, η_{opt} is simply

$$\eta_{\text{opt}} \cong \frac{1}{\theta} = \frac{V_{\text{eff}}}{V_{\text{app}}} \frac{2\beta fg}{a^{*2}}. \quad (37)$$

We therefore see that the parameter θ can be interpreted as an idealized inverse thermodynamic efficiency for the case where the advective current is small compared to the electromigration current.

Note that η_{opt} is highly dependent on the size of the pores and this dependence provides insight to the design of high-efficiency pumps. Figure 5 shows a plot of η_{opt} for both the exact formulation and the small-potential, second-order-accurate limit with nominal parameter values of $\zeta^* = -3.9$ and $\beta = 6.8$, and an ideal condition of $V_{\text{eff}} = V_{\text{app}}$. For the purpose of this plot, we therefore assume a relative constant zeta potential of $\zeta = -100$ mV. Although the overall trend of both solutions is similar, a discrepancy is apparent at small values of nondimensional pore sizes a^* . The peak η_{opt} of the numerical solution occurs at $a^* = 2.5$ as compared to a value of $a^* = 4.2$ for the approximated solution. Further, the second-order approximation underpredicts the increase in the conductivity of EDLs associated with finite values of φ^* , and therefore overpredicts the maximum efficiency by a factor of 1.2. For our electrolyte chemistries and the wall properties predicted by the zeta potential model, the $a^* = 2.5$ point of the numerical solution yields $\eta_{\text{opt}} = 6.5\%$. For instance, the numerical model suggests that 48-nm-diameter pores are optimal for 1 mM ion concentrations. The efficiency curves shown here are qualitatively similar to the

predictions of Chen and Santiago [18] for planar electrokinetic pumps.

The peak in the efficiency curve is a result of the competing effects of Joule heating (which dominates at large a^*) and reduced hydraulic power and higher current density at low a^* . We first consider the large a^* limit. To demonstrate the effect of viscosity and temperature, we define ion mobility as $\nu = u_d/F$ [29] which is a measure of the drift velocity u_d acquired by an ionic species subjected to a force F . Next, if we approximate ions as hard spheres with a characteristic Stokes diameter, d , defined as the diameter of a sphere in continuum fluid flow with a drag equal to that of the ion [29]. Under this approximation, the ion mobility is $\nu = 1/3\pi\mu d$ and the molar conductivity is $\Lambda = z^2 e^2 N_A / 3\pi\mu d$. For $a^* \gg 1$, $f \approx 1$ and $g \approx 1$, and from Eq. (37), efficiency becomes

$$\eta_{\text{opt}} = \frac{6\pi d \varepsilon(T)^2 \zeta(\text{pH}, n_{\infty}, T, \dots)^2}{a^2 z^2 e^2 n_{\infty}} \quad (a^* \gg 1), \quad (38)$$

where the parameters in parenthesis have been written to remind the reader that permittivity and zeta potential depend on at least several independent parameters such as temperature and the chemistry of the working electrolyte and the solid surface. This relation points out interesting functionalities. First, in this regime, thermodynamic efficiency is not a function of solvent viscosity and temperature dependent only through permittivity and zeta potential. Unless temperature drastically affects ion density (as it might in the case of chemical reactions in a weak electrolyte), ζ has only a weak dependence on temperature. Second, we see that larger ions (with associated lower molar conductivities and mobilities) are thermodynamically favorable as they impart the same force density into the flow with less Joule dissipation. For the same reason, ions with valences higher than unity are unfavorable. In the regime of thin EDLs, smaller pores are therefore favored and there is a decrease of η_{opt} as a^* increases. Higher conductivity yields higher current densities and lowers zeta potential (see Eq. (38) and Fig. 6) and is therefore also detrimental to thermodynamic efficiency. However, as discussed in Yao et al. [28], conductivity often has a lower limit dictated by practical considerations associated with pH stability. That is, for a given electrolyte buffer, lower ion concentration implies lower buffering capacity. Low buffering capacity can adversely affect pH in high-flow-rate, high-current applications and thereby affect zeta potential and overall pump performance.

For the large a^* regime, we can also use an approximate expression for ζ to express thermodynamic efficiency in terms of surface charge density. As discussed by Hunter [1], this expression follows from the PB equation as $\zeta = \sigma_s \lambda I_0(a^*) / (\varepsilon I_1(a^*))$ for small potentials. Substitution of this expression into Eq. (38) yields

$$\eta_{\text{opt}} \cong \frac{3\pi d \sigma_s^2 \varepsilon k T}{a^2 z^4 e^4 n_{\infty}^2} \quad (a^* \gg 1, \text{ small } \zeta^*). \quad (39)$$

This expression shows that the dependence of η_{opt} on ε is perhaps less important than suggested by Eq. (38) and em-

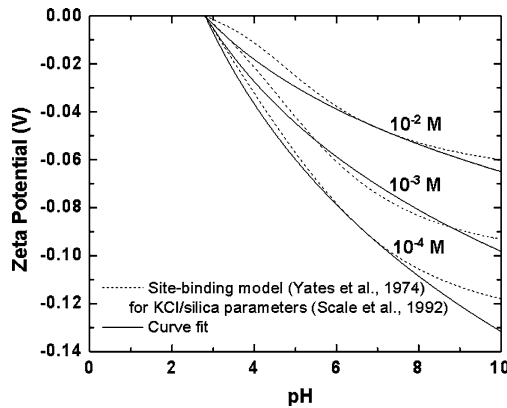


Fig. 6. Nonlinear fitting curve for the GCSG site-binding model for the zeta potential of KCl/silica interfaces. The curve fit shown is of the form $\zeta = (-0.058 \log_{10}(\text{pH}) + 0.026)(-\log_{10}(c_{\infty}))^{1.02}$ which gives values within 10% of the GCSG site-binding model prediction within the following range: $2.8 \leq \text{pH} \leq 10$, $10^{-4} \leq c_{\infty} \leq 10^{-2}$ M.

phasizes the importance of using monovalent ions to achieve high-efficiency pumps. Also, this expression shows the explicit dependence of η_{opt} on temperature and surface charge density, which is a strong function of pH and concentration [30].

At values of a^* of order unity and lower, the effects of finite EDLs dominate. In the regime of $a^* \ll 1$, using second-order-accurate series expansions for f and g , Eq. (37) yields

$$\eta_{\text{opt}} \cong \frac{3\pi d \zeta^2 a^2 z^2 e^2 n_{\infty}}{16k^2 T^2} \quad (a^* \ll 1, \text{ small } \zeta^*). \quad (40)$$

If we assume a constant zeta potential, this equation shows η_{opt} decreases as a^* decreases in the small a^* regime (see Fig. 5). This can be explained in terms of pressure work. Because of the no-slip condition at the wall, finite EDLs imply a significant deficit in mass flux as compared to the thin EDL “plug flow” case. This contributes to lower flow rate per unit area, lowering hydraulic power produced. Since pressure is a linear function of flow rate, pressure forces are accordingly decreased in this fully viscous liquid flow.

In addition to lower hydraulic power, channels with small a^* also typically have higher average current density since, at high zeta potentials, the conductivity of EDLs can be much higher than the bulk conductivity. For example, local ion conductivity near the wall for the prediction given by Eq. (19) is 34 times higher than the conductivity of the bulk electrolyte, as shown in Fig. 4b. At low a^* , both this and the hydraulic power reduction discussed above contribute to lower thermodynamic efficiency for decreasing a^* . Note that the model described here neglects ionic current in the “stagnant layer” of counterions immediately adjacent to the wall of the microchannel, as discussed by Lyklema et al. [31]. However, the effects of such ion conduction would further increase average current density in electrokinetic channels and therefore should not change the trends predicted by our model in the low a^* regime.

Lastly, we should note that the theoretical development given in this paper for flow rate, pressure, and efficiency of

electroosmotic pumping should be interpreted only as an approximation for values of a^* of less than about unity. The model uses a simple form of the Boltzmann equation which may result in inaccurate descriptions of the potential distribution (and therefore ion density distributions) for the case of overlapping charge double layers. Although such layers have recently been treated theoretically by Qu and Li [32] and Conlisk et al. [33], we believe that the theory for overlapping EDLs and associated models for the dependence of ζ on a^* has not yet been adequately developed. We are currently working on a model for electrokinetic flows with overlapping EDLs and will discuss this topic in a future paper.

2.4. Model for pH and ion density dependence of zeta potential

Zeta potential is a key parameter in the characterization of any EO pump system. Classical theory describes the EDL as divided into the Stern and Gouy–Chapman diffuse layers [2]. The Stern layer counterions are absorbed onto the wall, while the ions of the Gouy–Chapman layer are diffuse and therefore available to impart work on the fluid. The plane separating these two layers is called the shear plane, and the potential at this plane is the zeta potential, ζ . Combining the Boltzmann distribution of the EDL ions with the Poisson equation, Gouy–Chapman (GC) theory relates the zeta potential to the effective surface charge of the shear plane, which is a strong function of pH and a relatively weak function of ionic concentration.

Because of the immense difficulties in predicting the value of ζ from first principles, this parameter is typically an empirically determined value obtained using electroosmotic flow or streaming sodium tetraborate buffer general, difficult to determine, even for a fixed working fluid and surface material. However, as we discuss in Results, the value of ζ varies significantly with changes in the ionic concentration, c_{∞} , of the electrolyte. As pointed out by Yates et al. [30], applying a simple Gouy–Chapman diffuse EDL model leads to the erroneous conclusion that ζ scales with concentration as $c_{\infty}^{-0.5}$. Yates et al. [30] have presented an EDL model, called the site-binding model, on the basis of Gouy–Chapman–Stern–Grahame (GCSG) theory, which can be used to predict ζ across a significant range of pH and ionic concentration values for simple buffers on oxide surfaces. Their model separates the surface and buffer association/dissociation reactions of the EDL into those occurring on a layer immediately adjacent to the surface (below the inner Helmholtz plane, IHP) and a layer corresponding to the molecules further from the wall but unable to diffuse (above the outer Helmholtz plane, OHP). GCSG theory takes into account interfacial chemical reactions at the IHP (involving silanol groups at the surface and water ions) and the reactions which occur at the OHP (which involve water ions and the association/dissociation reactions of the electrolyte ions). This theory predicts a less pronounced (and more accurate)

dependence of zeta potential on bulk ionic concentration than the GC theory.

Scales et al. [34] have applied the model of Yates et al. [30] to the case of KCl electrolytes on silica surface. The site-binding model fits their experimental data very well given modeling parameters suggested by Scales. However, because of the nature of the equilibrium reaction formulations, it is difficult to derive an explicit formula for ζ based on their model. For our pump efforts, therefore, we have generated the following explicit relation for ζ as a function of pH and ion density by curve fitting to the model data presented by Scales:

$$\zeta = (-0.058 \log_{10}(\text{pH}) + 0.026)(-\log_{10}(c_{\infty}))^{1.02}. \quad (41)$$

This curve fit predicts the value given by the site-binding model to within 10% for ranges of ionic concentration of 10^{-4} to 10^{-2} M and pH values of 2.8 to 10. A comparison of this curve fit and the site-binding model results is shown in Fig. 6. In this paper, we apply the zeta potential model for silica/KCl interfaces as an approximate prediction of trends in our borosilicate/borate buffer pumps. One justification for this is that, as discussed earlier, we expect the buffers in our high zeta potential porous structures to act as symmetric electrolytes with the properties of the univalent sodium ion. A second justification of this is that the observed trends of zeta potential as a function of pH and concentration for silica and borosilicate are similar [35]. In Results, we quantitatively compare the trends we observed from our borosilicate-based EO pumps to the trends reported by Scales et al. [34] for silica surfaces with KCl.

3. Conclusions

We have developed analytical expressions for the electroosmotic flow rate, current, and thermodynamic efficiency for a porous structure EO pump operating under a pressure load. The model includes a numerical solution of the nonlinear Poisson–Boltzmann equation for electric potential and the coupling of this solution to the equations of fluid motion and ionic current. The model is valid for large zeta potential and accounts for the nonuniformity of ion conductivity across the flow areas of a porous pump. We treat our buffers as symmetric, monovalent electrolytes and leverage a single measurement of bulk liquid conductivity to account for the current contribution of all ions present in the buffer. The model uses determined pore sizes to predict absolute pressure performance. The model also leverages a curve fit of the GCSG site-binding model for KCl/silica interface to estimate the dependence of zeta potential on ionic density and pH in our borosilicate-based system. The model expresses pressure, flow rate, current, and thermodynamic efficiency of EO pumps as a function of quantifiable electrolyte properties and the properties of the electrical double layer. For the nondimensional surface potential thermodynamic efficiency curve predicts a maximum is a result of the effects of Joule

heating, which dominates the trend in efficiency at large a^* , and the effects of reduced hydraulic power and higher current density in the low a^* regime.

Lastly, we note that the Boltzmann equation is not directly applicable for overlapping EDL fields where the center potential associated with the wall charges is nonzero, and the ionic concentrations in the center of the pore are not necessarily equal to those of the original bulk concentration. Therefore, the solutions of the PB equation presented here may result in inaccuracy in our model for the thick EDL case (e.g., a^* less than about unity). We are currently developing an analytical model to account for the effects of overlapping EDLs.

Acknowledgments

This work was supported by DARPA under Contract F33615-99-C-1442 and by Intel Corporation.

Appendix A. Nomenclature

A	Cross-sectional area (m^2)
E_x	Electric field (V m^{-1})
F	Force (N)
I	Current (A)
L	Length (m)
L_e	Average length along the pore path (m)
N_A	Avogadro's number (mol^{-1})
P_x	Pressure gradient (Pa m^{-1})
ΔP	Pressure capacity (Pa)
Q	Flow rate (ml min^{-1})
T	Temperature (K)
V	Potential (V)
W_P	Pressure work (W)
\forall	Total volume of the porous medium (m^3)
\forall_e	Void volume of the porous medium (m^3)
a	Pore radius (m)
d	Sphere diameter (m)
c_{∞}	Electrolyte concentration (M)
e	Elementary charge (C)
i	Current density (A m^{-2})
k	Boltzmann constant (J K^{-1})
n_{∞}	Electrolyte number concentration (m^{-3})
r	Radial coordinate (m)
u	Velocity (m s^{-1})
z	Charge number (–)
Λ	Molar conductivity ($\text{S m}^2 \text{mol}^{-1}$)
β	Nondimensional advective current parameter (–)
ε	Permittivity of liquid ($\text{C V}^{-1} \text{m}^{-1}$)
η	Thermodynamic efficiency (–)
θ	Nondimensional efficiency parameter (–)
λ	Debye length (m)
μ	Viscosity (Pa s)
ν	Mobility ($\text{m s}^{-1} \text{N}^{-1}$)

$\rho(r)$	Charge density at a point distance r from the axis (C m^{-3})
$\sigma(r)$	Conductivity at a point distance r from the axis (S m^{-1})
σ_∞	Electrolyte conductivity (S m^{-1})
σ_s	Surface charge density (C m^{-2})
φ	Electrical potential (V)
ζ	Zeta potential (V)
τ	Tortuosity (–)
ψ	Porosity (–)

Subscripts

adv	Advection
app	Applied value
eff	Effective value
em	Electromigration
max	Maximum value
opt	Optimal value
p	Single pore
+	Cation
–	Anion

References

- [1] R.J. Hunter, Zeta Potential in Colloidal Science: Principles and Applications, Academic Press, London, 1981.
- [2] R.F. Probstein, Physicochemical Hydrodynamics, 2nd ed., Wiley, New York, 1994.
- [3] L. Jiang, J.C. Mikkelsen, J.-M. Koo, D. Huber, S. Yao, L. Zhang, P. Zhou, J.G. Maveety, R. Prasher, J.G. Santiago, T.W. Kenny, K.E. Goodson, IEEE Trans. Comp. Packag. Manufact. Technol. 25 (3) (2002) 347.
- [4] J.E. MacNair, K.C. Lewis, J.W. Jorgenson, Anal. Chem. 69 (1997) 983.
- [5] Y. Fintschenko, A. van den Berg, J. Chromatogr. A 819 (1998) 3.
- [6] V. Pretorius, B.J. Hopkins, J.D. Schieke, J. Chromatogr. A 99 (1974) 23.
- [7] F. Theeuwes, J. Pharmaceutical Sci. 64 (12) (1975) 1987.
- [8] F. Theeuwes, U.S. Patent 3,923,426, 1975.
- [9] Y. He, W. Gan, Chinese Patent 97212126.9, 1998.
- [10] W. Gan, L. Yang, Y. He, R. Zeng, M.L. Cervera, M. de la Guardia, Talanta 51 (2000) 667.
- [11] P.H. Paul, D.J. Rakestraw, U.S. Patent 6,019,882, 2000.
- [12] C. Yan, U.S. Patent 5,453,163, 1995.
- [13] M.C. Oborny, P.H. Paul, K.R. Hencken, G.C. Frye-Mason, R.P. Manginell, U.S. Patent 6,224,728, 2001.
- [14] P.H. Paul, D.J. Rakestraw, D.W. Arnold, K.R. Hencken, J.S. Schoeniger, D.W. Neyer, U.S. Patent 6,277,257, 2001.
- [15] S. Zeng, C.H. Chen, J.C. Mikkelsen, J.G. Santiago, Sens. Actuat. B 79 (2–3) (2001) 107.
- [16] S. Zeng, C.H. Chen, J.G. Santiago, J. Chen, R.N. Zare, J.A. Tripp, F. Svec, J. Fréchet, Sens. Actuat. B 82 (2–3) (2001) 209.
- [17] S. Yao, D. Huber, J.C. Mikkelsen, J.G. Santiago, in: Proc. ASME IMECE Microfluidics Symposium, New York, 2001.
- [18] C.H. Chen, J.G. Santiago, J. Microelectromech. Systems 11 (6) (2002) 672.
- [19] D.J. Laser, S. Yao, C.H. Chen, J.C. Mikkelsen, K.E. Goodson, J.G. Santiago, T. Kenny, in: Proc. Transducers '01, Munich, 2001.
- [20] P. Mazur, J.Th.G. Overbeek, Rec. Trav. Chim. 70 (1951) 83.
- [21] C.L. Rice, R. Whitehead, J. Phys. Chem. 69 (1965) 4017.
- [22] E.J.W. Verwey, J.Th.G. Overbeek, Theory of Stability of Lyophobic Colloids, Elsevier, Amsterdam, 1948.
- [23] W.R. Bowen, F. Jenner, J. Colloid Interface Sci. 173 (1995) 388.
- [24] P. Moin, Fundamentals of Engineering Numerical Analysis, Cambridge Univ. Press, Cambridge, UK, 2001.
- [25] E.W. Washburn, Physics 7 (1921) 115.
- [26] F.A. Morrison, J.F. Osterle, J. Chem. Phys. 43 (1965) 2111.
- [27] D.R. Lide, CRC Handbook of Chemistry and Physics, 76th ed., CRC Press, Boca Raton, FL, 1995.
- [28] S. Yao, D.E. Hertzog, S. Zeng, J.C. Mikkelsen, J.G. Santiago, in press.
- [29] J.O'M. Bockris, A.K.N. Reddy, Modern Electrochemistry: Ionics, 2nd ed., Plenum, New York, 1970.
- [30] D.E. Yates, S. Levine, T.W. Healy, J. Chem. Soc. Faraday Trans. 74 (1974) 1807.
- [31] J. Lyklema, S. Rovillard, J. DeConinck, Langmuir 14 (20) (1998) 5659.
- [32] W. Qu, D. Li, J. Colloid Interface Sci. 234 (2000) 397.
- [33] A.T. Conlisk, J. McFerran, Z. Zheng, D. Hansford, Anal. Chem. 74 (9) (2002) 2139.
- [34] P.J. Scales, F. Grieser, T.W. Healy, Langmuir 8 (1992) 965.
- [35] T.W. Healy, L.R. White, Adv. Colloid Interface Sci. 9 (1978) 303.